A Cartilage-inspired Multidimensional Sensor with High Elasticity and Anisotropy Based on a Segmented Embedded Strategy

Haocheng Jiang [a,b], Saihua Jiang [a,b,*], Guohua Chen [a],Yang Lan [c]

[a] Institute of Safety Science and Engineering, School of Mechanical and Automotive Engineering, South China University of Technology, Guangzhou 510641, P. R. China

[b] Guangdong Provincial Key Laboratory of Technique and Equipment for Macromolecular Advanced Manufacturing, South China University of Technology, Guangzhou 510641, P.R. China

[c] Dept of Chemical Engineering, University College London, London WC1E 7JE, U.K.

Abstract

Flexible, stretchable and sensitive multidimensional sensing systems that can decouple different mechanical inputs and identify multidimensional signals are crucial for dynamic human signal perception and intelligent human-computer interaction. Most of the reported multidimensional sensors are suitable for discriminating in-plane deformation directions, and the sensing materials are difficult to balance between stretchability and mechanical strength. Here, we propose a segmented embedded structure strategy inspired by the interlaced structure of cartilage. This strategy balances the performance of reinforced composites with flexibility and the high toughness and enables us to construct a wearable multidimensional sensing system that can sense planar strain/pressure. The multidimensional sensing system exploits the inherent anisotropy and layered structure design of composites to decouple the sensing functions. Supported by machine learning algorithms, the high accuracy demonstration of the multidimensional sensors in typical multidimensional motion joint posture monitoring and recognition confirms their potential in practical applications such as personal health sensing and human-computer interaction.

Introduction

Recently, there has been renewed interest in flexible materials and devices that can sensitively and accurately detect various types of stimuli to achieve skin-like multimodal sensing functions[1-3]. Due to their excellent mechanical properties and multi-axis sensing characteristics, flexible wearable sensors can collect and convert multimodal physiological signals or multidimensional motion signals from the human body or other soft carriers[4-6]. They can provide dynamic monitoring and feedback directly or indirectly, and have a wide range of applications in personalized medicine[7], health detection[8], sports monitoring[9], human-computer interaction[10] and other fields. Much of the previous research has focused on optimizing the performance parameters of single-axis sensors[11], such as sensitivity, response time and sensing range, by using conductive fillers[12] or structural design[13] to fabricate high-performance flexible sensors. However, these traditional sensors can only measure single or limited stimuli due to structural coupling, and cannot fully reflect the multidimensional stimulus signals in complex and dynamic environments. The limitation of a single response may also cause signal loss or error, restricting its practical applications such as human dynamic motion, intelligent bionic robots, etc.

Multidimensional sensing systems that can distinguish various directions of stimuli or different types of responses are indispensable for dynamic human motion sensing and complex behaviour monitoring[14]. In most cases, conventional flexible sensors cannot accurately identify the direction or stimuli due to isotropy and structural coupling effects, where strain in one direction causes deformation in three directions[15]. To solve the above problem, a growing body of literature suggests that unique anisotropic structural materials can eliminate the interference of deformation in different directions and realize directional sensing through structural decoupling[2, 15, 16]. Other strategies to distinguish and detect external load characteristics, and achieve multidirectional strain sensing or multifunctional sensing properties include multi-layer stacking[17] or cross-shaped geometric design[18], new electrode materials[19] or constructing sensor arrays with local strain-insensitive rigidity[20], etc. The approach of building a sensing system by integrating multiple sensors, each responsible for a single-dimensional response, can also eliminate signal interference with each other. Although anisotropic structures are the key to directional sensing, most sensors based on anisotropic structures have a strain sensing range limited to about 30%[21], which is insufficient for detecting

complex motion modes with large strain and multiple degrees of freedom. Therefore, besides solving the decoupling problem of multidimensional sensing, designing stretchable structures is equally important.

Natural protein-mineral nano-composite materials with both flexibility and intrinsic anisotropy have superior mechanical properties[22], such as cartilage, nacre, and wood. Cartilage tissue is a remarkable soft connective tissue that consists of a protein matrix with a large number of collagen fibres that are arranged in parallel or cross-linked patterns[23, 24]. The special interlocking structure gives it both the rigidity of fibre orientation and the adhesion and elasticity of the soft matrix (Figure 1A). Inspired by this structure, the topological entanglement polymer network achieved a combination of high elastic strain and high toughness, expanding the performance space of materials[25]. The segmented interlocking structure design enhanced the multi-scale superior performance of materials from macro to micro, which can be applied in the fields of mechanical regulation[26], additive manufacturing[27], shock absorption[28] and so on nanocomposites. The soft matrix around the hard fibres protects them from the peak stress of external loads and bears a large contribution of elastic strain[22]. These characteristics enable it to adapt to different mechanical stresses and load changes, which are required for multidimensional sensing applications.

In this study, inspired by the natural interlaced structure of cartilage, we developed a simple strategy to improve the mechanical properties of segmented embedded structures. And the intrinsic anisotropy of the embedded structures was utilized to achieve structural decoupling and to construct multidimensional sensors that could sense and accurately identify tensile and compressive strains in orthogonal directions in the plane. To demonstrate the structural strategy, we constructed enhanced composites that balance softness and high toughness by designing macroscopic segmented structures. As an example, the segmented embedded structures were fabricated by combining polyacrylamide gel (PAAm), a soft material with excellent viscoelasticity, as the matrix part and wood, a natural biomaterial with a layered porous structure similar to collagen fibre bundles, as the template for the hard part (Figure 1A). The soft segments contributed to the elastic deformation, while the hard parts supported a large amount of load through stress dispersion and local deformation. The soft and hard segment materials were tightly adhered to by macroscopic mechanical topology and hydrogen bonding, which enhanced the overall ductility and preserved the partially anisotropic structure of the embedded materials. This enabled their application as in-plane

sensing units in complex scenarios. A multidimensional sensing system with a locally highly aligned conductive network was demonstrated by vertically stacking segmented embedded unit sensors and polydimethylsiloxane as an interlayer. The system could sense strains in multiple dimensions, and independent responses to strain changes in different directions and identification of strain intensity directions were evaluated and analyzed by detecting electrical signals. The accuracy of data recognition was improved by using machine learning and classification algorithms. The system was capable of monitoring physiological signals and dynamic human motion effectively.

Results and discussion

Synthesis and Morphology

Herein, segmented embedded hydrogels (SEH) were prepared via a three-step strategy: pre-treatment of the hard material, impregnation of the soft material, and design of the segmented embedded hydrogels (Figure 1B). The chemically treated wood was used as a carrier for the hard segments due to its anisotropic structure, similar to that of collagen fibres[29]. The natural wood is brownish with stiff cell walls and large vessels[30]. After spatial delignification using an efficient method (Figure S1), cracks and voids appear in the areas of cell intersection, increasing the porosity between the wood tube walls. Lignin is mainly concentrated in the cell corners and intercellular layers[30]. By removing most of the lignin and hemicellulose here, the tight junctions between the fibres can be released, allowing space for the impregnation of the soft material and maintaining the inherent orientation of the cellulose nanofibres (CNF)[31]. This change in the microstructure is particularly evident in the scanning electron microscopy images (SEM), where the dissolution of the cell wall after delignification is visible, and the pores are then filled with soft gel and tightly bound together (Figure 1B). Furthermore, small pore tube cavities were observed on the surface of the wood along the direction of growth (Figure S2), which allowed the gel chains to penetrate the cellulose skeleton and strengthen the adhesive bond between the wood and the gel. The segmented embedded hydrogel was designed as macroscopically alternating soft and hard structures that locally retain the anisotropy of the hard parts and allow them to stretch like soft materials. In this case, the soft segment consists of polymerized cross-linked acrylamide chains (PAAm) and the hard segment consists of the wood hydrogels (WH) composed of oriented cellulose nanofibres and in-situ polymerised polyacrylamide. Not only does PAAm acts as a filler to penetrate the treated wood

frame, but it also acts as a binder to create a strong interaction between the cellulose cell wall and the soft segments.

The composition and chemical structure of segmented embedded hydrogels, particularly the hard parts, were comprehensively studied. Compared to the natural basswood, the lignin content decreased to 17.6% after the first stage of alkali treatment and to 9.1% after the second stage of acidic sodium chlorite treatment (Figure S3). And the sample treated with acidic $NaClO_2$ alone was used as the control group with a lignin content of 15.1%. When treated with alkali at mild temperatures, OH^- weakens the hydrogen bonds between cellulose and hemicellulose and saponifies the ester bonds between hemicellulose and lignin[32], effectively dissolving the hemicellulose and small amounts of lignin. The chemical reaction between sodium chlorite and glacial acetic acid produces a strong oxidant, ClO_2, which oxidizes the benzoquinone structure and the conjugated double bonds of the side chains in the lignin[33]. The aromatic structure forms acidic groups which underwent oxidative ring-opening reactions, leading to the dissolution and removal of the lignin.

Fourier Transform Infrared (FTIR) spectroscopy was demonstrated to further confirm the above constituent and chemical structure changes (Figure S4). All samples showed cellulose absorption peaks at 3340 cm^{-1} (-OH stretching) and 1032 cm^{-1} (-C-O stretching)[34], with characteristic peaks for the lignin component at 1506 cm^{-1} and 1593 cm^{-1} (benzene skeleton vibration), which disappeared significantly after chemical treatment. Furthermore, the peak at 1733 cm^{-1} (stretching vibration of the acetyl group of the hemicellulose backbone)[35] was also significantly reduced after alkali treatment. The absorption peak associated with -OH appeared red-shifted, indicating the formation of the hydrogen bond between PAAm and CNF[36]. These results all support the removal of most of the lignin and the increased interaction between the exposed cellulose fibres and the PAAm gel and which is a good basis for the subsequent designed material for mechanical strength and stability.

Mechanical Property

Careful characterization of the mechanical properties was carried out to understand the deformability and mechanical performance of the segmented embedded hydrogel. Figure 2A showed the tensile stress-strain curves for the SEH, soft PAAm hydrogel and hardwood hydrogel. Through macroscopic structural design, SEH incorporates the merits of the elasticity of soft materials and the toughness of hard materials, exhibiting excellent mechanical properties with elongation damage (400%) an order of magnitude greater than hard WH (R-direction 30%) and

tensile strength (0.3MPa) three times that of soft PAAm (0.1MPa). The hard section WH displays unique anisotropic mechanical properties, for example, the strength in the L-direction (7.8 Mpa) was several times higher than in the R-direction (1.1 Mpa), accompanied by a loss of flexibility of only 3% strain (Figure S5). The tensile strength of WH follows the same upward trend as the hydrogel cross-linker content increases, but the strain of WH remains essentially stable at 30% (R-direction) due to the limitation of the high-strength oriented cellulose backbone (Figure S5). PAAm exhibits typically elastic material properties with low tensile strength but extremely high elasticity, stretching up to 400%.

The soft-hard segment embedding structure was designed using the contributions of a soft matrix and hard fibres, and the adhesion between the two interfaces of the structure was a key factor in good macroscopic performance[25]. The influence of crosslinking density of soft gel and orientation of wood on interfacial adhesion was investigated by conducting tensile tests on samples with different soft-hard arrangements. It was found that decreasing the crosslinker content led to higher elasticity of soft segment gel and increased tensile elongation (Figure S6). Moreover, lower crosslinker content resulted in higher interfacial adhesion strength (Figure 2B), which could be ascribed to the reduced crosslinking degree of the gel, the decreased entanglement between PAAm chains, and consequently the enhanced hydrogen bonding between free PAAm chains and lignin-free cellulose backbone. The interface junction is the fracture site for all samples, as stress is dispersed in the hard segment material and concentrated at the interface, where bonds in the high-stress concentration area break preferentially, resulting in macroscopic fracture. Furthermore, parallel-oriented SEH showed higher fracture stress than vertical-oriented SEH. This could be attributed to the honeycomb-like arrangement of wood, which causes a small shrinkage strain in the direction of wood growth, lowering transverse shear stress. The interfacial adhesion is mainly achieved by a combination of mechanical interlocking[37] and hydrogen bonding (Figure 2C). The naturally porous structure of cellulose allows the gel precursor to form a key-lock topological structure in the pores after polymerization. Moreover, after lignin removal, the cellulose surface became rich in hydroxyl groups[29], which interact with gel via hydrogen bonding, enhancing interfacial viscosity. The interfacial adhesion facilitates smooth stress transfer between phases and the deformation involved overcoming both the elasticity of soft gel and the interaction with the cellulose backbone.

The length ratio and arrangement design of the soft and hard segments were other important factors to consider. The ratio of soft segment length to total length was defined as a. Figures 2D and E present the stress-strain curves for various soft segment ratios, with schematic diagrams of gel samples in the insets. And Figure 2F summarises the effect of soft segments on fracture stress and strain. It was observed that increasing the soft segment ratio resulted in higher tensile strain and lower fracture stress, which could be attributed to the fact that in this arrangement it was mainly the soft segment that underwent elastic deformation and stress concentration. Considering that the gel had a satisfactory overall tensile strength and could match the strain of human joint motion[38], a soft segment ratio of a=1/3 was selected for subsequent studies as it exhibited a high modulus of elasticity in the range of 200% strain. The tensile behaviour of the composites was also influenced by embedding rigid materials of varying lengths in the soft matrix. The ratio of hard segment length in the middle to total length was defined as b. Figures 2G and H show that composites with aligned segments have similar mechanical properties regardless of segment length, as indicated by their comparable moduli and low-strain tensile curves. Composites with differently oriented segments showed different mechanical responses, with higher elongation and tensile strength for vertical than parallel segments, following the same trend as varying soft segment ratios a. And tensile strength increased initially and then decreased as the aspect ratio of the hard segments increased (Figures 2I). To investigate the specific role of the hard and soft segment composition on the stretching process, the stress distribution images of the simulated tensile process were shown in Figure 3A (Horizontal arrangement) and Figure S7 (Vertical arrangement). The hard segment material experienced larger stress, which was concentrated on the interface of soft and hard segments, and the soft segment exhibited the main strain along the tensile direction. Due to the special anisotropic structure of wood, the hard segment structure along the tensile direction had extreme rigidity[39], making it resistant to deformation. However, shear stress on the interface perpendicular to the tensile direction induced small strain, which was observed on the interface in the SEM image (Figure 3A). Moreover, under high strain conditions (>200%), the parallel arrangement of the hard part embedded in the middle curled could be attributed to the shear force and vibration of the tensile machine. Curling did not occur in samples with vertical orientation, as the dense wood structure in this direction could withstand greater shear stress without deformation (Figure S8). Figure 3B presents the change in sample width-projected length, illustrating the relationship between deformation and strain.

Samples with vertical orientation showed almost no deformation, whereas samples with horizontal orientation showed a sudden change at ε = 150%. Therefore, samples with horizontal orientation were generally maintained in the 150% strain range, to ensure the stability of segmented embedded gel in subsequent applications.

To demonstrate the contribution of each segment to the overall strain, strain changes in hard and soft segments during stretching were investigated. The strains in the soft and hard segments were denoted as ε_s and ε_h, respectively, and they had different growth rates as the composite was stretched. Figure 3C showed that the main strain was ε_s due to the large modulus difference between the material of the soft segment and the hard segment. The strain in the soft segment was difficult to drive the stretching of the hard segment, especially when arranged horizontally, as there was almost no strain along this direction in the wood structure, with ε_h being around 2%. The contribution of each segment to the total strain was summarised as $\varepsilon = \phi_s*\varepsilon_s+\phi_h*\varepsilon_h$, where ϕ_s and ϕ_h were the volume ratios of the soft and hard segments in the whole material, and the contribution rate was $f_s = \phi_s*\varepsilon_s/\varepsilon$, $f_h = \phi_h*\varepsilon_h/\varepsilon$. When oriented horizontally, the soft segment contributes almost constantly above 98%. When oriented vertically, the contribution of the soft segment increases with ε and stabilises at 96% at about ε = 150%, after which the soft segment cannot deform the hard segment further (Figure 3D).

The mechanical properties of the segmented embedded hydrogel were further analysed using the stress-strain curves of loading and unloading, where Figure 3E showed the curve with maximum strain increase at b = 1/3. When loaded to a low strain and then unloaded, as in Figure 3E with ε_{max} = 100%, the loading and unloading curves overlapped, indicating almost complete elasticity. And when loaded to a high strain, the curve showed a noticeable hysteresis loop, implying that there was a limit to the elastic strain of loading and unloading. The elastic limit strain ε_e was defined as the strain at which the hysteresis ratio W_D/W exceeded 2%, where W_D was the dissipated work (the area of the hysteresis loop), W was the tensile work (the area under the loaded curve), and W_E was the elastic work (the area under the unloaded curve) (Figure S9). W_D/W was a dimensionless measure of hysteresis, $W=W_D+W_E$. PAAm hydrogels have high elastic strains due to the entropic elasticity of the long polymer chains and the low viscosity of water and Wood hydrogels exhibit low elastic strains due to the dense entanglement of cellulose chains and the stiffness of the hard segment network[40]. As shown in Figure 3F, SEH exhibited a distinct hysteresis peak at 150% strain,

and different hard segment ratio distributions followed a similar trend. These results demonstrate the satisfactory mechanical properties of SEH for tensile applications, while the particular structural design provides the basis for anisotropic multidimensional applications. The good mechanical properties reveal the great potential of the proposed hydrogel structure and properties for sensing applications.

On the basis of the tensile model (Figure S10), the mechanical performance of composites can be improved by the addition of an optimum amount of reinforcement phase in the soft matrix[41]. A high aspect ratio of hard segments can also compensate for soft segment softness and increase overall composite strength[22]. In this case, the mechanical properties of composite materials are enhanced by arranging hard structures with anisotropic orientation in a staggered mode in a flexible matrix. The performance improvement mechanism can be elucidated as follows (Figure 3G): when the composite material undergoes stretching, the polymer chains in the soft segment network are initially elongated, accommodating a large amount of elastic deformation. The load is primarily transferred through the topological interlocking between the hard segment and the soft matrix, which are strongly bonded. As the tensile stress increases, the strain of the soft segment disperses high stress to the hard segment, while the soft material embedded in the hard material transfers load among the oriented hard fibres by stretching and shearing, indicating that the hard segment collectively sustains most of the tensile load. Moreover, due to the anisotropic characteristics of the hard material, it can achieve small-scale deformation along the direction perpendicular to the alignment (Figure 3G (i) (ii)). This implies that the localized stress at the adhesive interface can be dispersed to the entire hard segment by compression or tensile deformation of the hard segment, resulting in high-stress dispersion and elastic energy dissipation.

Characterization of the Sensing Performance

To demonstrate the reliability of SEH in sensing applications, its transport capability was evaluated by adding NaCl ions to the gel system. The conductive paths in the gel system were influenced by the deformation in each direction due to Poisson's ratio, which affected the ion transport efficiency. The anisotropic structure of the gel system enabled the decoupling of the conductive network and the realization of directional sensing under various directional loads[14]. Firstly, the electrical performance of WH is anisotropic, as shown in Figure S11. The resistance in the L-direction is about 2/3 of that in the R-direction. This can be attributed to the anisotropic structure of wood,

which facilitates ion transport along the cellulose fibre orientation without crossing the cell wall barrier. Additionally, the sieve tube structure of the wood also enhances ion transport. The conductivity of WH increases with ion content, which is consistent with other conductive hydrogels[31, 42-44]. The ionic conductivity of the gel system was enhanced by the carboxyl groups on the surface of CNF, which facilitated the ion migration[45]. The SEH exhibited anisotropic conductivity at the macroscopic level, similar to WH, owing to its embedded anisotropic local structures. The resistivity of the horizontal hard segment along the direction of wood growth is lower than that of the other segments (Figure 4A). Linear stretching of the sensor increased the conductive path and decreased the cross-sectional area, resulting in reduced conductivity and increased resistance with strain[1]. Figure 4B showed the sensitivity (gauge factor, GF) at b=1/2 for the vertical hard segment and the maximum strain increase curve. The GF values were 6.92 (strain <150%) and 21.98 (strain >150%). The GF was defined as $GF=(\Delta R/R_0)/\varepsilon=(R-R_0)/R_0/\varepsilon$, where R_0 was the initial resistance without strain, ε was the linear strain and R was the resistance under strain. To enable the sensor to be applied to most human joint parts, the structural design with the highest GF_1 at ε<150% was chosen so that the strain range could cover most movements. The sensor could effectively and reliably monitor human movements such as finger bending, neck twisting and knee joint movement, providing useful data for health detection and disease prevention. Figure 4C summarised the difference in sensitivity of different structures. GF_1 generally increased with the proportion of hard segment material. The unusual change at b=1 may be due to natural variations in wood structure, as wood has a lower resistivity at rest (Figure 4A), indicating more active ion movement so that strain has a relatively greater effect on its ion transport.

The sensing performance of the SEH sensor was further evaluated, including cyclic response at different strains and frequencies, long-term stability and response time. The sensor was cyclically stretched to 25%, 50%, 75% and 100% strains and showed good stability over this range, as indicated by the stepped peaks and stable waveforms at each strain (Figure 4D). The sensor also responded similarly to different loading frequencies at the same strain, with ΔR remaining stable at 100% when a periodic 50% strain was applied at 0.25Hz, 0.5Hz, 1Hz and 2Hz respectively (Figure 4E). The fast response and recovery of the sensor were verified as essential parameters for its validity as a sensing element. Figure 4F showed that the sensor exhibited rapid reaction to small external mechanical stimuli, with strain response times of 93 ms and 136 ms respectively, indicating

its remarkable ability to react and relax quickly. The long-term operation of the sensor was investigated by monitoring its relative resistance variation over 600 cycles of strain release. The variation was largely stable and the signal response was consistent around cycles 3, 300 and 600 respectively, as shown by the insets (Figure 4G). These results demonstrate the excellent reliability of the SEH sensor for practical applications. The segmental embedded structure of the sensor enables a stable and sensitive signal under various mechanical stimuli, suggesting its potential for human joint monitoring and medical detection.

Multidimensional Sensing and Wearable Applications

Flexible sensors are used as input terminals for wearable monitoring systems, converting mechanical stimuli into electrical signals and providing the basis for the interaction process. SEHs are applied to construct multidimensional sensors that can monitor motion in multiple degrees of freedom and the device structure is shown in Figure 5A. The sensing device consists of a three-layer structure that responds to different stimuli in three dimensions. The top and bottom layers are vertically aligned SHE, an in-plane uniaxial sensor based on a highly aligned network that enables directional strain sensing. The middle layer is bonded by hydrophilic-modified PDMS (Figure S12) and the local sandwich structure senses spatial pressure stimuli and generates capacitive signals. Benzophenone abstracts hydrogen atoms from the methyl groups on the PDMS surface under UV light irradiation, generating a large number of free radicals. These free radicals initiate the polymerization of the gel on the PDMS surface, resulting in a strong bonding[37]. The anisotropic structure of the rigid segmental gel and the PDMS as a dielectric layer prevents stress effects between the top and bottom layers, as confirmed by finite element stress distribution simulations (Figure S13). When the device is deformed in the direction of orientation of either the top or bottom layer, the hard segment of the material bears most of the load and the strain is mainly concentrated in the soft segment of the layer, without affecting the deformation of the other layer (Movie S1). By constructing a sandwich structure multi-axis strain sensor, strains in multiple dimensions can be measured simultaneously. The sensor devices are attached to the skin surface of the joint area in a crossed pattern to detect different types of joint movement. The different directions of movement produce different strain states in the device, which correspond to electrical signals from the sensors in each dimension. The directional variability of the resistive signal sensitivity is shown in Figure S14, where the y-sensor has almost no signal change with GF_y=0.013 when the x-sensor is

directionally stretched along the x-axis. The value of the directional sensing difference $\Delta GF = GF_x - GF_y$ is 6.481 for both XY orientations. The resistance ΔGF shows the directional behaviour of the loading direction. These results suggest that the directional difference in in-plane strain can be calculated by differentiating the change in resistance and that the unknown magnitude and direction of the applied strain can be predicted from the known output.

Next, the multidimensional signal sensor was tested for its function in monitoring human joints in Figure 5B. For example, when the head was nodded up and down, the Y-direction had a large strain amplitude and the X-direction had a small strain amplitude (Figure 5B (i)). This change in strain state resulted in a large signal change in the y-sensor and a small signal change in the x-sensor. When the neck was rotated left and right, the X-sensor had a greater change than when nodding, but the Y-sensor had a much smaller change. Ideally, the compressive strain would cause a negative change in resistance, but in reality, the skin on the neck did not deform in a single direction, and the lateral movement showed a small tensile strain instead of a significant compressive strain. The multidimensional sensors placed at the shoulder and wrist could also distinguish joint movements in different directions. The signals in the X and Y directions were almost identical when the swinging arm moved forward and backwards. The relative resistance in the Y-direction increased sharply as the shoulder moved outwards and was almost negligible in the X-direction (Figure 5B (ii)). The wrist sensors also showed significant directional differences during bending and twisting. And repeated signal waveforms prove that the multidimensional sensor device can accurately detect the cross-directional movement of joint parts (Figure 5B (iii)).

The stability and effectiveness of the z-directional capacitive sensing signal were also verified. When the z-sensor was pressed, the capacitive signal changed due to the change in thickness of the dielectric layer, indicating its ability to sense different pressures (Figure S15). The pressure sensing of the z-sensor was also applied to Morse communication, based on the different duration and intensity of pressure variations corresponding to the "dot" and "dash" signals (Movie S2). The Morse code of "SCUT" was represented in real-time by the changes in the pressure capacitance signal (Figure 5B (iv)). Without pressure, the capacitor signal was only slightly affected by stretching the resistive sensor (Figure S16). This can be attributed to the different effects of stretching the conductive and dielectric layers. The stretching alters the ion transport in the conductive layer, but has almost no effect on the dielectric layer, as shown in Figure S12. Therefore,

the response of the Z-sensor, which reflects the capacitor signal, is negligible. The above demonstration confirms that the SEH-based multidimensional sensor can clearly and accurately differentiate strain in three directions, facilitating its functional application in posture detection and joint health prevention.

The performance of our multidimensional sensor for joint motion monitoring was further evaluated by experimenting with using skipping as a test case. Skipping rope is a popular aerobic exercise that involves multiple joints and requires good coordination and posture, but it can also cause bone or muscle injury if done incorrectly. The sensor was attached to different joints of the participants and the sensor data was collected using a multi-channel resistance tester. The data was then sent to a mobile phone via Bluetooth for real-time display and analysis. The shoulder and wrist, which have complex motion characteristics, were equipped with the multidimensional sensor, and the knee, which has mainly one-dimensional motion, was equipped with the SEH sensor. The five sensor motion parameters that were collected from the three joint sites for the different skipping postures are shown in Figure 6A and Movie S3. Detailed sensor data for each posture are shown in Figure 6B, where the regular signal changes of the corresponding sensors indicate the force and state of the joint site. Different skipping postures were analysed using sensor data and their impact on physical health and exercise performance was assessed. Resistance sensors were attached to the skippers' knees, wrists and shoulders to measure their joint angles and range of motion. Figure 6B illustrates how different skipping postures were reflected in the sensor data. i) shows an incorrect posture characterised by excessive knee flexion and normal wrist rotation. A significant change in resistance was indicated by the knee sensor (green), while the wrist sensor showed a regular signal. In contrast, the knee sensor showed negligible resistance changes in other postures when the knee was kept straight or slightly bent. iv) shows another incorrect posture characterised by excessive arm opening and arm swinging. Corresponding regular resistance changes were shown by the shoulder sensors (purple and blue). ii) and iii) show postures namely wrist swing and wrist-arm swing. It was found that correct skipping postures could reduce joint stress and injury risk while enhancing skipping efficiency.

Machine learning, a technique that excels at handling multi-channel data, was utilized to further perform joint state recognition (Figure 6C). The Kruskal-Wallis test was applied to rank the features before the analysis (Figure S17) and several typical machine learning optimization algorithms were

tested (Figures S18-S21). Five-fold cross-validation was used to train all the algorithms and to avoid overfitting. The highest recognition accuracy of 98.7% was achieved by the non-linear support vector machine algorithm based on the quadratic kernel function (Figure S22), and the confusion matrix of the classification results is shown in Figure 6D. However, this algorithm was only validated for the prepared multidimensional sensor device for skipping rope joint posture recognition under small data collection. These experimental results demonstrate the effectiveness of the SEH-based multidimensional sensor in collecting strain-sensing data in multiple directions and monitoring joint motion state and posture.

Conclusion

In this paper, inspired by the structure of articular cartilage tissue, We propose a segmented embedded strategy that combines soft and hard materials in a topological and zipper-shear chain manner. This strategy improves the ductility of the composite material while preserving the anisotropy of the hard segments. Polyacrylamide hydrogel was used as the soft matrix and delignified wood as the hard template to demonstrate this strategy. We tune the adhesion strength and the ratio of soft and hard segments to achieve a stretchability of 150% elastic strain, which covers most large strain scenarios. A multidimensional sensing system with local anisotropy based on the segmented embedded materials was designed through a three-layer structure that responds to different stimuli in three dimensions. The sensor can independently detect multi-directional strain variations and pressure changes in the plane, enabling real-time and continuous monitoring of multidimensional motion states of joints with large strains and multiple degrees of freedom. Different motion postures and joint motion states are successfully classified and recognized with a high accuracy of 98.7% using a second-order kernel SVM machine learning algorithm. The segmented embedded structure strategy provides a novel solution for improving the performance of other polymer materials. Moreover, the multidimensional sensor and its application in joint motion detection demonstrate the potential of wearable health monitoring devices.

Methods

Materials

Unless otherwise mentioned, all chemicals were purchased from Macklin and used without further purification. Basswood was supplied by Wood Veneer Company. Chemical treatment agents: Sodium hydroxide (NaOH, >98%), Sodium chlorite ($NaClO_2$, >80%), Glacial acetic acid ($C_2H_4O_2$, 99.5%). Monomer: Acrylamide (AAm). Crosslinker: N, N' - Methylene bisacrylamide (MBAA). Initiators: Ammonium persulphate (APS). Polydimethylsiloxane (PDMS) was purchased from Dow Corning SYLGARD™ 184. Isopropanol and benzophenone (BP) were obtained from Shanghai Aladdin Biochemical Technology Co., ltd. The solvents used were ethanol alcohol and deionized water.

Preparation of the Hard segment

First, the natural wood samples (0.5mm thickness wood veneers) were immersed in 10 wt% NaOH solution at 70℃ for 30 minutes to remove hemicellulose and some lignin. After washing the wood samples with deionized water to neutralize, the treated wood was immersed in 2 wt% $NaClO_2$ solution at pH=4.6 and boiled for 30 minutes to remove lignin and then repeated washing with deionized water. The delignified wood turned white and was stored in ethanol alcohol.

Preparation of Segmented Embedded Hydrogel

The AM solution was prepared to contain MBAA and 0.02g of APS (0.67 wt% of AM) in 7g of deionized water which was based on the amount of AM (3g). After sufficient stirring, the delignified wood was immersed in AM solution for more than 3h at room temperature. The samples were taken out and arranged in a certain shape between two glass plates and filled with uncrosslinked AM solution. After that, the crosslinking was completed under ultraviolet light (20W) for 10 minutes.

Preparation of Multidimensional Sensor

Adding 1M NaCl to the uncrosslinked AM solution and stirring it to make it completely dissolved, then immersing the wood template. Then repeat the above experimental operation to complete the preparation of the conductive segmented embedded hydrogel.

PDMS film was prepared by mixing Sylgard 184 host and curing agent at 10:1. The PDMS of size $10 \times 10 \times 2$mm was soaked in 10 wt% benzophenone solution (solvent: ethanol) for 3 min and

rinsed with isopropanol gently. After the PDMS was air-dried, the PMDS and segmented embedded hydrogels were assembled in a sandwich structure. In the middle, AM solution was used as the binder, which was also crosslinked under UV light for 10mins.

Characterization

The standard method of lignin estimation (ICS 65.020.01 “Standard method for analysis of forestry biomass-Determination of structural polysaccharides and lignin”) was followed to determine the lignin content. The morphology of delignified wood and segmented embedded hydrogel were characterized using a field emission scanning electron microscope (Merlin, Germany Zeiss) after freeze-drying. The chemical structure was analyzed by Fourier Transform Infrared spectrometer (FT-IR, Nicolet IS50) and X-ray diffractometer (XRD, Rigaku Ultima IV). Uniaxial tensile tests of the samples were performed by using a universal testing machine (CMJ4000, China) with a 1 kN load cell. Before the tests, all samples were cut into 30mm × 10mm × 0.5mm. The tests were performed at a tensile velocity of 100 mm/min at ambient conditions. A humidifier was used during the cyclic tensile test to prevent hydrogel dehydration. The samples of the stress-strain test were performed at least five times. The electrical properties of the hydrogel were recorded by using a digital bridge instrument (East Tester, ET4401) and a digital multimeter (LinkZill TruEbox 01RC, China). The gauge factor was measured by calculating the resistance changes ($\Delta R/R_0$) of the samples as follows: $\Delta R/R_0=(R-R_0)/R_0\times 100\%$, where R_0 and R are the initial resistance and the one after applying strain to the samples, respectively.

Data availability

The data that support the findings of this study are available from the corresponding authors upon request.

Reference

1. Lei, M. et al. Breathable and Waterproof Electronic Skin with Three-Dimensional Architecture for Pressure and Strain Sensing in Nonoverlapping Mode. *Acs Nano* **16**, 12620-12634 (2022).
2. Zhang, F. et al. Anisotropic conductive networks for multidimensional sensing. *Mater Horiz* **8**, 2615-2653 (2021).
3. Amjadi, M., Kyung, K.U., Park, I. & Sitti, M. Stretchable, Skin-Mountable, and Wearable Strain Sensors and Their Potential Applications: A Review. *Adv Funct Mater* **26**, 1678-1698 (2016).
4. Khan, Y., Ostfeld, A.E., Lochner, C.M., Pierre, A. & Arias, A.C. Monitoring of Vital Signs with Flexible and Wearable Medical Devices. *Adv Mater* **28**, 4373-4395 (2016).
5. Wang, Y. et al. Recent advancements in flexible and wearable sensors for biomedical and healthcare applications. *J Phys D Appl Phys* **55** (2022).
6. Trung, T.Q. & Lee, N.E. Flexible and Stretchable Physical Sensor Integrated Platforms for Wearable Human-Activity Monitoring and Personal Healthcare. *Adv Mater* **28**, 4338-4372 (2016).
7. Gu, Y.D. et al. Mini Review on Flexible and Wearable Electronics for Monitoring Human Health Information. *Nanoscale Res Lett* **14** (2019).
8. Gao, J.W. et al. Ultra-Robust and Extensible Fibrous Mechanical Sensors for Wearable Smart Healthcare. *Adv Mater* **34** (2022).
9. Khalid, M.A.U. & Chang, S.H. Flexible strain sensors for wearable applications fabricated using novel functional nanocomposites: A review. *Compos Struct* **284** (2022).
10. Liao, X.Q. et al. Hetero-contact microstructure to program discerning tactile interactions for virtual reality. *Nano Energy* **60**, 127-136 (2019).
11. Lei, Z.Y., Wang, Q.K., Sun, S.T., Zhu, W.C. & Wu, P.Y. A Bioinspired Mineral Hydrogel as a Self-Healable, Mechanically Adaptable Ionic Skin for Highly Sensitive Pressure Sensing. *Adv Mater* **29** (2017).
12. Pang, Y. et al. Epidermis Microstructure Inspired Graphene Pressure Sensor with Random Distributed Spinosum for High Sensitivity and Large Linearity. *Acs Nano* **12**, 2346-2354 (2018).
13. Chen, B.D., Zhang, L., Li, H.Q., Lai, X.J. & Zeng, X.R. Skin-inspired flexible and high-performance MXene@polydimethylsiloxane piezoresistive pressure sensor for human motion detection. *J Colloid Interf Sci* **617**, 478-488 (2022).
14. Yang, R.X. et al. Multimodal Sensors with Decoupled Sensing Mechanisms. *Adv Sci* **9** (2022).
15. Luo, N.Q. et al. Hollow-Structured G raphene-Silicone-Com posite-Based Piezoresistive Sensors: Decoupled Property Tuning and Bending Reliability. *Adv Mater* **29** (2017).
16. Li, Y.H. et al. Enhanced Potassium-Ion Storage of the 3D Carbon Superstructure by Manipulating the Nitrogen-Doped Species and Morphology. *Nano-Micro Lett* **13** (2021).
17. Pyo, S., Lee, J., Kim, W., Jo, E. & Kim, J. Multi-Layered, Hierarchical Fabric-Based Tactile Sensors with High Sensitivity and Linearity in Ultrawide Pressure Range. *Adv Funct Mater* **29** (2019).
18. Chen, H.T. et al. Omnidirectional Bending and Pressure Sensor Based on Stretchable CNT-PU Sponge. *Adv Funct Mater* **27** (2017).
19. Wu, Y.T., Yan, T., Zhang, K.Q. & Pan, Z.J. Flexible and Anisotropic Strain Sensors Based on Highly Aligned Carbon Fiber Membrane for Exercise Monitoring. *Adv Mater Technol-Us* **6** (2021).
20. Lee, J.H. et al. Heterogeneous Structure Omnidirectional Strain Sensor Arrays With Cognitively Learned Neural Networks. *Adv Mater* (2023).
21. Lee, J.H. et al. Highly Aligned, Anisotropic Carbon Nanofiber Films for Multidirectional Strain Sensors with Exceptional Selectivity (vol 29, 1901623, 2019). *Adv Funct Mater* **29** (2019).
22. Ji, B.H. & Gao, H.J. Mechanical properties of nanostructure of biological materials. *J Mech Phys Solids* **52**,

1963-1990 (2004).
23. Karamanos, N.K. et al. A guide to the composition and functions of the extracellular matrix. *Febs J* **288**, 6850-6912 (2021).
24. Halper, J. Basic Components of Connective Tissues and Extracellular Matrix: Fibronectin, Fibrinogen, Laminin, Elastin, Fibrillins, Fibulins, Matrilins, Tenascins and Thrombospondins. *Adv Exp Med Biol* **1348**, 105-126 (2021).
25. Liu, X. et al. Topoarchitected polymer networks expand the space of material properties. *Nat Commun* **13** (2022).
26. Li, Z. et al. Enhanced Mechanical Properties of Graphene (Reduced Graphene Oxide)/Aluminum Composites with a Bioinspired Nanolaminated Structure. *Nano Lett* **15**, 8077-8083 (2015).
27. Gu, G.X. et al. Three-Dimensional-Printing of Bio-Inspired Composites. *J Biomech Eng-T Asme* **138** (2016).
28. Zhou, X.Q., Yu, D.Y., Shao, X.Y., Zhang, S.Q. & Wang, S. Research and applications of viscoelastic vibration damping materials: A review. *Compos Struct* **136**, 460-480 (2016).
29. Kong, W.Q. et al. Muscle-Inspired Highly Anisotropic, Strong, Ion-Conductive Hydrogels. *Adv Mater* **30** (2018).
30. Postek, M.T. et al. Development of the metrology and imaging of cellulose nanocrystals. *Meas Sci Technol* **22** (2011).
31. Chen, C.C. et al. Highly strong and flexible composite hydrogel reinforced by aligned wood cellulose skeleton via alkali treatment for muscle-like sensors. *Chem Eng J* **400** (2020).
32. Garcia, J.C. et al. Search for optimum conditions of wheat straw hemicelluloses cold alkaline extraction process. *Biochem Eng J* **71**, 127-133 (2013).
33. Liu, H.M., Feng, B. & Sun, R.C. Acid-Chlorite Pretreatment and Liquefaction of Cornstalk in Hot-Compressed Water for Bio-oil Production. *J Agr Food Chem* **59**, 10524-10531 (2011).
34. Yaddanapudi, H.S., Hickerson, N., Saini, S. & Tiwari, A. Fabrication and characterization of transparent wood for next generation smart building applications. *Vacuum* **146**, 649-654 (2017).
35. Rana, R., Langenfeld-Heyser, R., Finkeldey, R. & Polle, A. FTIR spectroscopy, chemical and histochemical characterisation of wood and lignin of five tropical timber wood species of the family of Dipterocarpaceae. *Wood Sci Technol* **44**, 225-242 (2010).
36. Zhao, J.M. et al. Hierarchical Porous Cellulosic Triboelectric Materials for Extreme Environmental Conditions. *Small Methods* **6** (2022).
37. Yang, J.W., Bai, R.B., Chen, B.H. & Suo, Z.G. Hydrogel Adhesion: A Supramolecular Synergy of Chemistry, Topology, and Mechanics. *Adv Funct Mater* **30** (2020).
38. Chen, S.Q. et al. Superstretching MXene Composite Hydrogel as a Bidirectional Stress Response Thixotropic Sensor. *Acs Appl Mater Inter* **13**, 13629-13636 (2021).
39. Xiao, S.L. et al. Lightweight, strong, moldable wood via cell wall engineering as a sustainable structural material. *Science* **374**, 465-471 (2021).
40. Kim, J., Zhang, G.G., Shi, M.X. & Suo, Z.G. Fracture, fatigue, and friction of polymers in which entanglements greatly outnumber cross-links. *Science* **374**, 212-+ (2021).
41. Jager, I. & Fratzl, P. Mineralized collagen fibrils: A mechanical model with a staggered arrangement of mineral particles. *Biophys J* **79**, 1737-1746 (2000).
42. Yan, G.H. et al. Catechol-based all-wood hydrogels with anisotropic, tough, and flexible properties for highly sensitive pressure sensing. *Chem Eng J* **427** (2022).
43. Geng, L.H. et al. Muscle-inspired double-network hydrogels with robust mechanical property, biocompatibility and ionic conductivity. *Carbohyd Polym* **262** (2021).
44. Chen, C.C. et al. Toward Strong and Tough Wood-Based Hydrogels for Sensors. *Biomacromolecules* **22**, 5204-

5213 (2021).
45. Ye, Y.H., Zhang, Y.F., Chen, Y., Han, X.S. & Jiang, F. Cellulose Nanofibrils Enhanced, Strong, Stretchable, Freezing-Tolerant Ionic Conductive Organohydrogel for Multi-Functional Sensors. *Adv Funct Mater* **30** (2020).

Acknowledgements

This work was supported by the National Natural Science Foundation of China (22175066, 52274232) and the Natural Science Foundation of Guangdong Province (2023A1515012961).

Author contributions

Haocheng Jiang: conceptualization, methodology, visualization, formal analysis, investigation, data curation, and writing-original draft. Saihua Jiang: conceptualization, writing-review & editing, project administration, funding acquisition, and supervision. Guohua Chen: writing-review & editing, and supervision. Yang Lan: writing-review & editing, and supervision.

Competing interests

There are no conflicts to declare.

Materials & Correspondence

Correspondence to the author: Saihua Jiang.

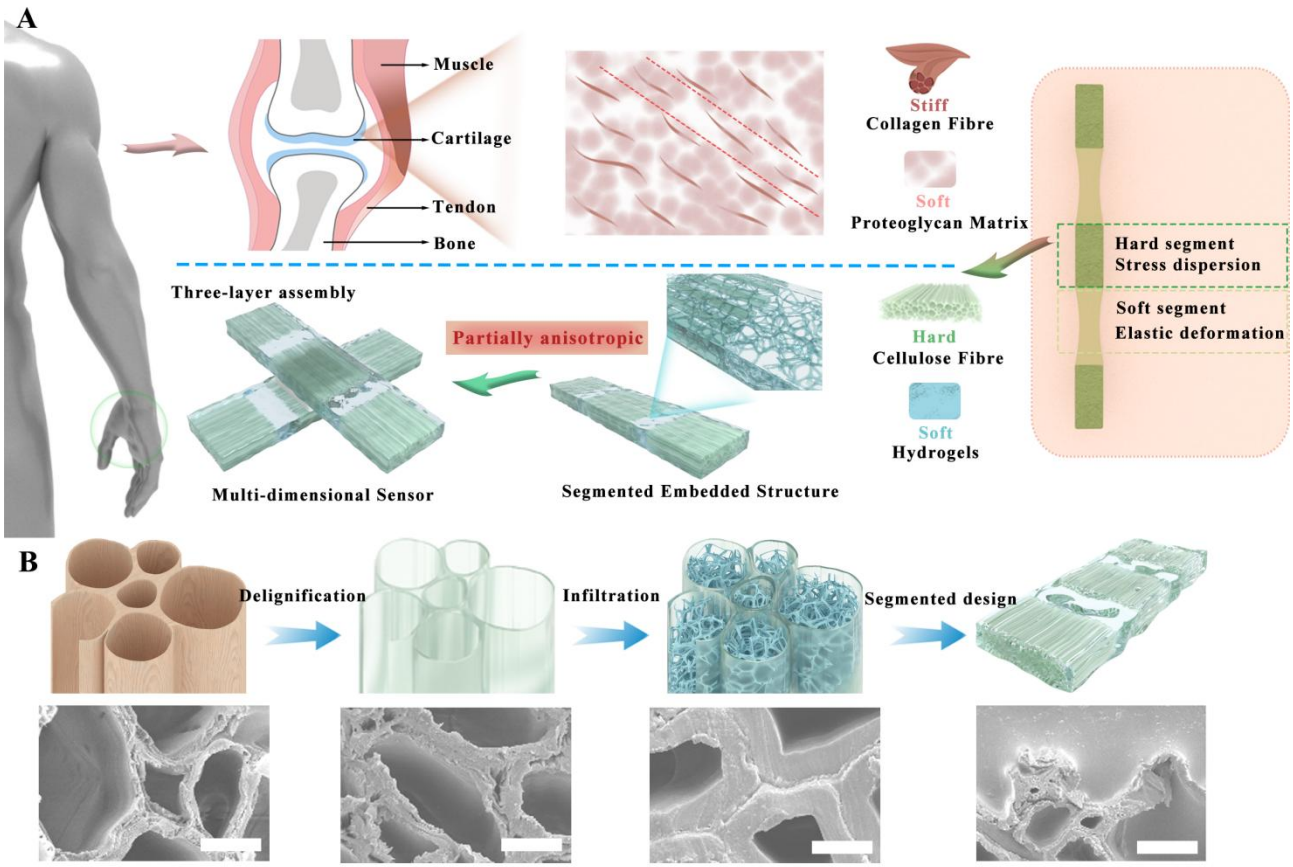

Figure 1. Design and application concept of the segmented embedded hydrogel.

A Segmented embedded structure strategy inspired by articular cartilage tissue, multidimensional sensor fabrication and its application in joint motion sensing. Articular cartilage consists of a soft protein matrix and hard collagen fibre bundles embedded within it, which enable it to withstand elastic strain and stress dispersion respectively. A similar structure is achieved by embedding hard cellulose fibres into PAAm hydrogel, forming segmented embedded hydrogels, and assembling them into a cross-linked three-layer configuration, with a hydrophilic-treated PDMS layer in the middle.

B Schematic illustration of the preparation process of segmented embedded hydrogels: delignification of wood fibres, impregnation of soft gel, and segmentation of structure design. The SEM images of each processing step are shown below, scale bar: 15μm.

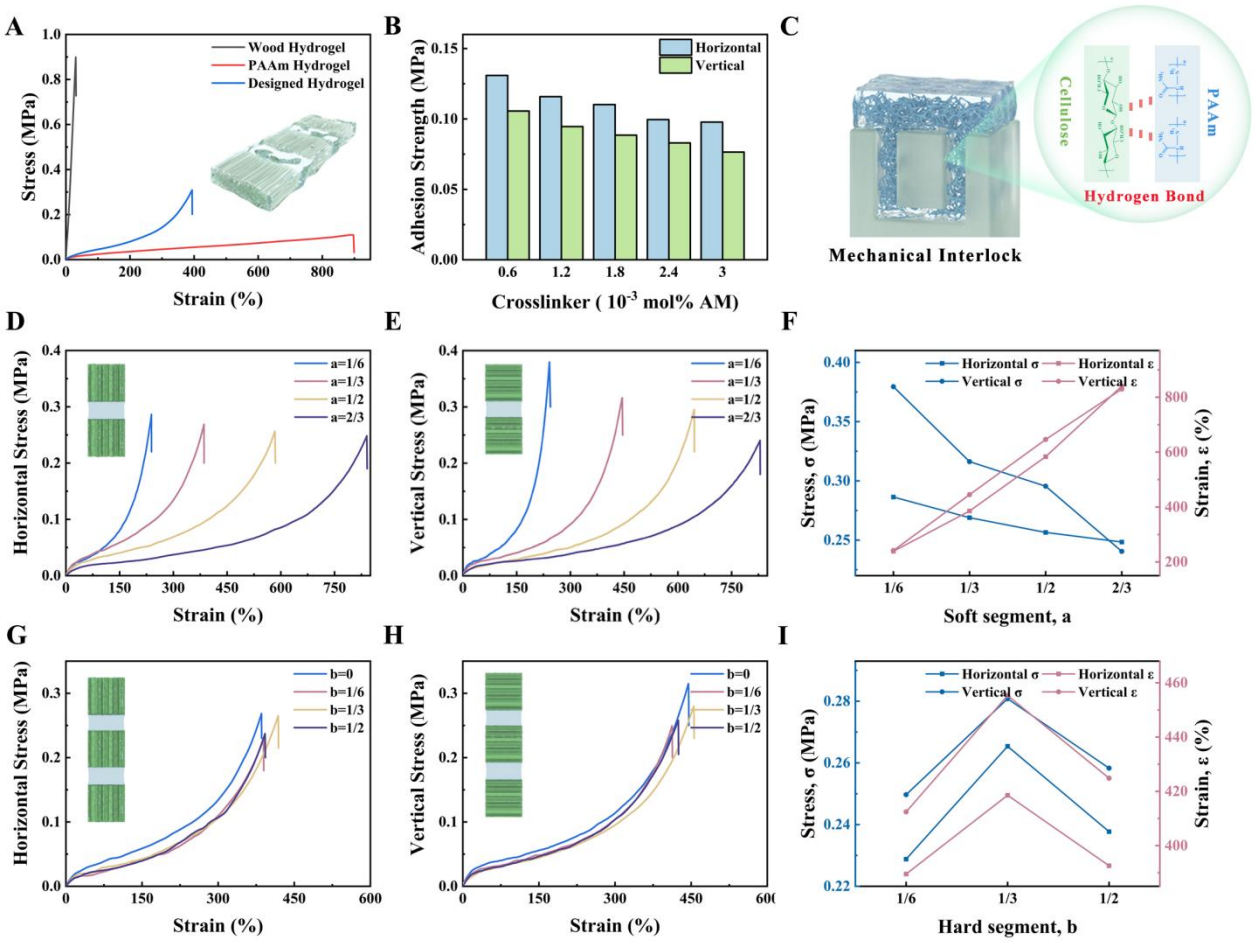

Figure 2. Mechanical properties of segmented embedded hydrogels.

A Tensile stress-strain curves of soft PAAm hydrogel, hardwood hydrogel and segmented embedded hydrogel. **B** Interfacial adhesion strength between soft and hard segments of materials with different crosslinker contents. **C** Schematic illustration of the interfacial adhesion mechanism between soft and hard segments, involving mechanical interlocking and hydrogen bonding. Stress-strain curves for segmented gels with varying soft segment fractions: **D** Vertical alignment of hard segments **E** Horizontal alignment of hard segments **F** Comparison of ultimate strain and fracture stress. Stress-strain curves for segmented embedded hydrogels with varying hard segment fractions: **G** Vertical alignment of hard segments **H** Horizontal alignment of hard segments **I** Comparison of ultimate strain and fracture stress.

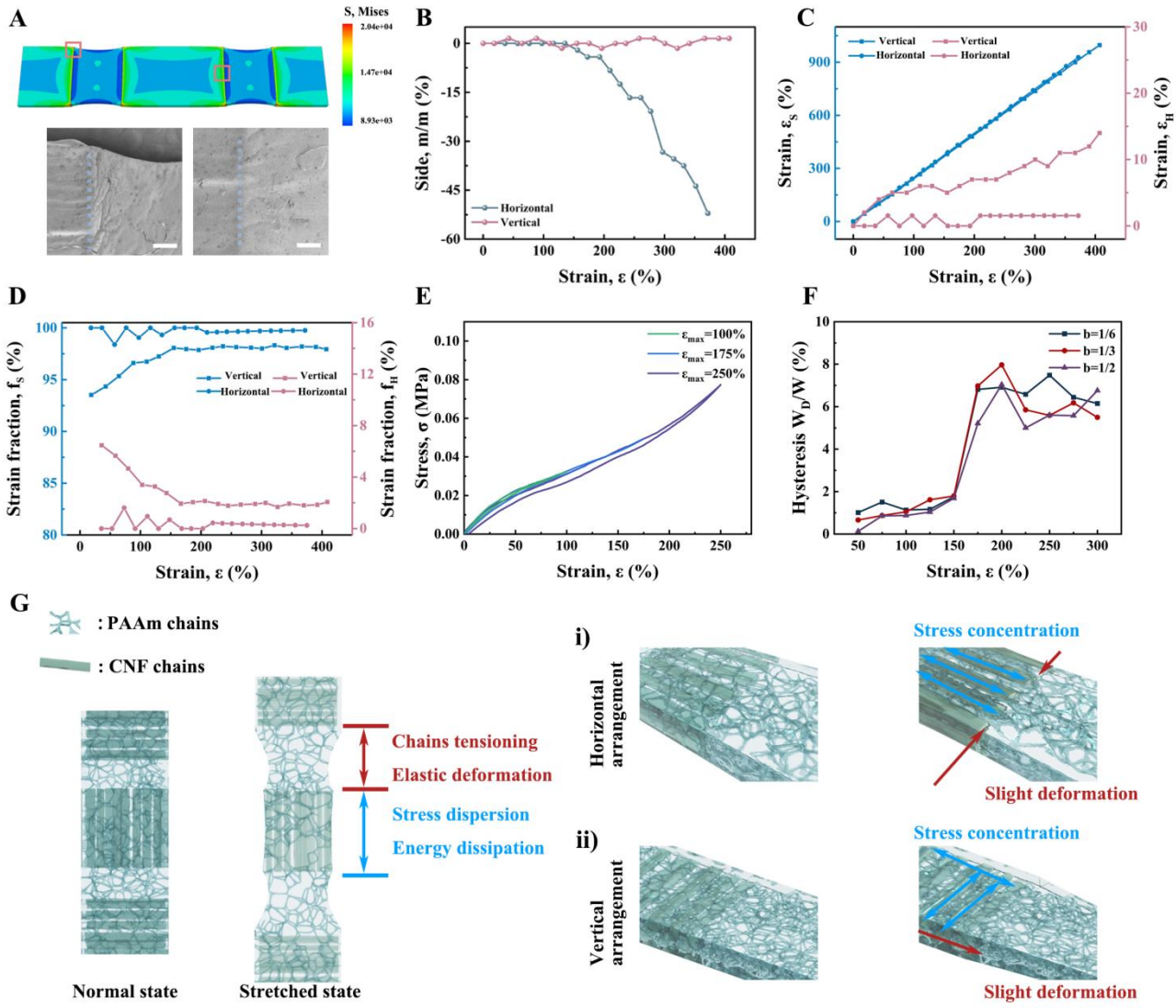

Figure 3. Deformation contribution analysis of segmented chimeric hydrogels.

A Simulated stress distribution of SEH under tensile deformation, with SEM images of the interface edge and centre between soft and hard segments shown in the lower insets, marked by blue dashed lines. The scale bar: 200μm. **B** The relative change in width projection length of tensile samples. **C** The variation of soft segment strain ε_s and hard segment strain ε_h concerning total strain. **D** The variation of soft segment strain contribution f_s and hard segment strain contribution f_h concerning total strain. **E** Loading-unloading stress-strain curves for b=1/3 at maximum strains of 100%, 175%, and 250%. **F** Summary of ultimate elastic strains for SEH. Where, the ratio W_D/W is a dimensionless measure of hysteresis. **G** Mechanical properties improvement mechanism, i) horizontal arrangement ii) vertical arrangement schematic representation of the tensile structure.

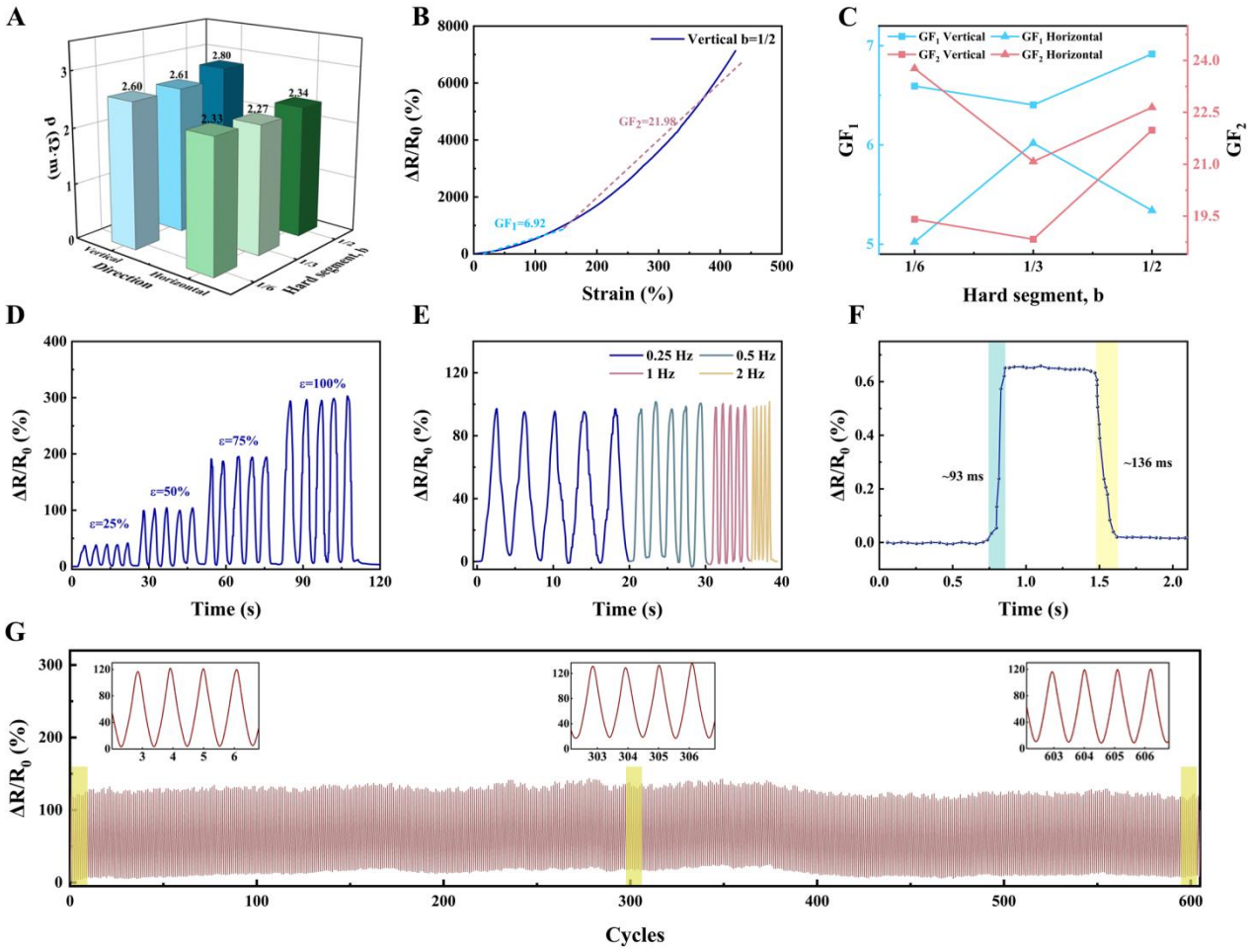

Figure 4. The electrical sensing performance of segmented chimeric hydrogel sensors.

A Resistivity law of SEH sensor. **B** Relative resistance change of sensor corresponding to tensile strain when b=1/2. **C** Summary of sensitivity GF and its dependence on segmentation design. **D** Resistance response of sensor at various strains (ε= 25%, 50%, 75%, 100%). **E** Resistance response of sensor at ε=50% for different loading frequencies (0.25Hz, 0.5Hz, 1Hz, 2Hz). **F** Strain response time of sensor for small strain changes. **G** Fatigue test of the sensor, subjected to cyclic stretching to 50% and releasing to initial state for 600 cycles.

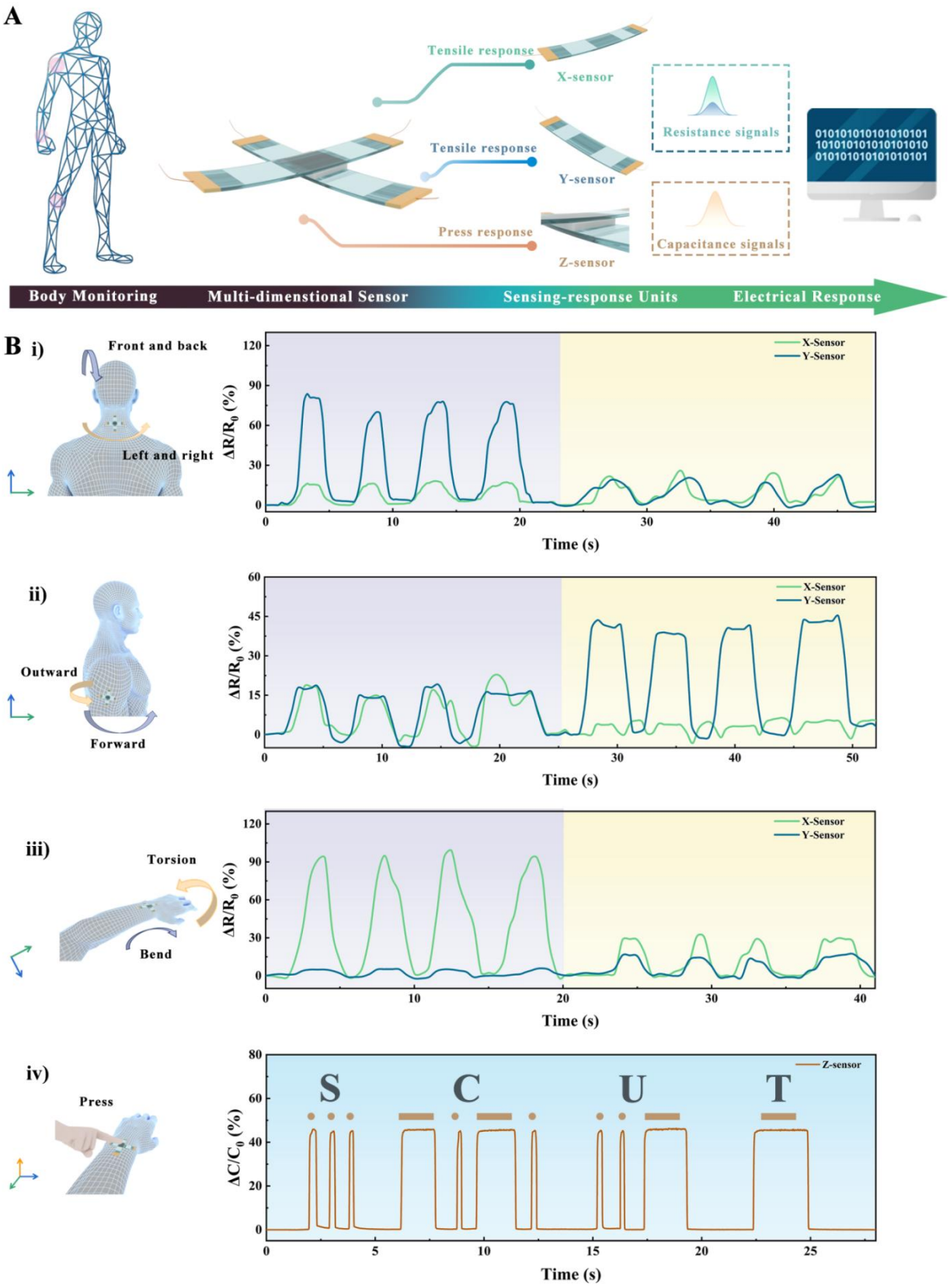

Figure 5. Fabrication and sensing application of multidimensional sensor devices.

A Schematic illustration of a multidimensional sensor device: a three-layer structure consisting of

cross-aligned SEH layers on top and bottom, and a hydrophilic-treated PDMS layer in the middle. The upper and lower layers provide strain-resistance responses in two orthogonal directions in the plane, while the middle layer serves as a dielectric layer for a pressure-capacitance response. **B** Sensing application of multidimensional sensor device at various human joint locations, including i) forward and backward movement and left and right movement of the neck; ii) forward extension and outward expansion movement of the shoulder; iii) bending and twisting movement of the wrist; iv) pressing action at the middle position. Specifically, iv) shows the generation of Morse code "SCUT" by using the pressure-capacitance signal.

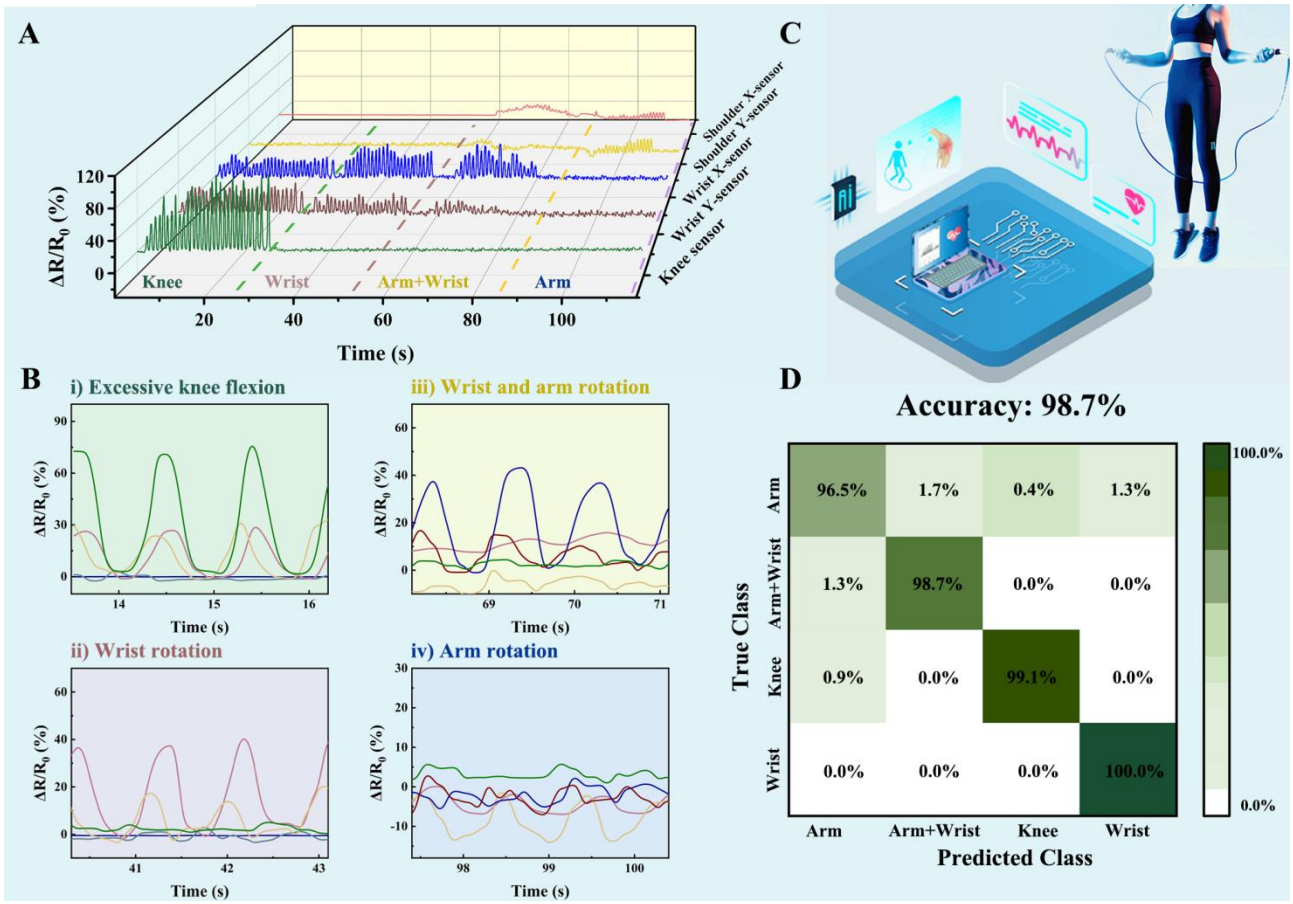

Figure 6. Application of multidimensional sensor for monitoring and identifying joint motion patterns and abnormal conditions.

A Resistance response of shoulder, wrist, and knee joints during skipping rope exercise. **B** Signal responses of selected joint motion patterns, including i) excessive knee flexion-incorrect posture; ii) wrist rotation-correct posture; iii) wrist and arm rotation-incorrect posture; iv) arm rotation-incorrect posture. **C** Data processing and joint motion classification using a computer program. **D** Confusion matrix for joint motion classification using machine learning, with an accuracy of 98.7%.